



Spatiotemporal variability of drought/flood and its teleconnection with large-scale climate indices based on standard precipitation index: a case study of Taihu Basin, China

Dingkui Wang¹ · Zengchuan Dong¹ · Feiqing Jiang¹ · Shengnan Zhu¹ · Zihan Ling¹ · Jiayi Ma¹

Received: 15 October 2021 / Accepted: 17 February 2022 / Published online: 28 February 2022
© The Author(s), under exclusive licence to Springer-Verlag GmbH Germany, part of Springer Nature 2022

Abstract

With the intensification of global warming, frequency of floods and droughts has been increasing. Understanding their long-term characteristics and possible relationship with large-scale meteorological factors is essential. In this study, we apply signal denoising, dimensionality reduction technique, and wavelet transform to study the spatiotemporal distribution pattern of drought/flood and its teleconnection with large-scale climate indices. Based on the precipitation data of 63 hydrological stations in the Taihu Lake Basin (TLB) for 54 years from 1965 to 2018, the standard precipitation index (SPI) was used as an indicator. The ensemble empirical mode decomposition (EEMD) and empirical orthogonal function (EOF) methods were used to explore the spatiotemporal evolution characteristics of droughts and floods. In addition, the cross-wavelet transform (XWT) method was used for teleconnection analysis. The results indicated that during 1965–2018, the SPI of the TLB showed quasiperiodic oscillations dominated by interannual oscillations (52.5%). Except for the trend of drought in spring, the basin showed a wetter trend at annual, summer, autumn, and winter scales. There were two main spatial modes (total 78.48% contribution) in the TLB, consistent across the region and reverse distributed from south to north. The dry areas were mainly in southern Zhexi and the northern Huxi sub-regions; the Hangjiahu and Yangchengdianmao sub-regions were prone to flooding. In addition, SPI was correlated with various large-scale meteorological factors, but the strength of the correlation had specific temporal and spatial heterogeneity. The research results can provide TLB reference values for water resource management and flood/drought disaster control.

Keywords Meteorological drought/flood · Drought index · Multiple time scale · Climate variability · Teleconnection patterns · Cross-wavelet transform · Response analysis

Introduction

According to the AR6 report of the Intergovernmental Panel on Climate Change (IPCC), the global surface temperature has increased by 0.84–1.1 in the past 120 years (IPCC 2021), and there is a continuing trend. At the same time, this warming trend is accompanied by frequent extreme climate events (Pei et al. 2020). Drought lasts for a long time and affects a large area (AghaKouchak et al. 2015; Philip et al. 2017; Yu et al. 2021); floods are frequent and destructive (Khan

et al. 2021). Drought and flood disasters have always had many adverse effects on the ecological environment and economic development worldwide and made up some of the most severe meteorological disasters (Arduino et al. 2005; Salehnia et al. 2020). There have been many studies on the analysis of drought and flood characteristics in various regions of the world (Vasileios et al. 2018; Yang and Scanlon 2019). Both drought and flood are made up of imbalances in water availability (Paulo et al. 2016). Grasping the development laws and causes of drought and flood is of indelible significance to alleviate disasters, reduce economic losses, and maintain sustainable development.

Based on the characteristics of drought and flood events, it is challenging to identify and evaluate the level of drought and floods (Wang et al. 2020a). Therefore, different indices have been proposed regularly to judge drought and flood grades. Currently, the commonly used indices include the

Responsible editor: Marcus Schulz

✉ Zengchuan Dong
zcdong@hhu.edu.cn

¹ College of Hydrology and Water Resources, Hohai University, Nanjing 210098, China

standardized precipitation index (SPI) (Mckee et al. 1993), Palmer drought severity index (PDSI) (Palmer 1965), and self-calibrating Palmer drought severity index (scPDSI) (Wells et al. 2004), standardized precipitation evapotranspiration index (SPEI) (Vicente-Serrano et al. 2010), effective drought index (EDI) (Byun and Wilhite 1999), etc. The advantages and disadvantages of various drought and flood indicators in use can be found described in previous studies (Hayes et al. 1999; Li et al. 2019). Compared with other indices, the SPI has the advantage of multiple timescales, which can better reflect the variation in drought and flood characteristics at different scales (Guttman 1999). The merit of the SPI is the ease of computation, which is reflected in data acquisition. By only considering the precipitation factor as space–time adaptive (Hui et al. 2014), the computation only needs to collect precipitation data, which is popular in areas where meteorological data are scarce, so the SPI is widely used throughout the world (Byun and Kim 2010; Salehnia and Ahn 2022). Much research has been done on the spatiotemporal characteristics of drought and flood in critical areas based on the SPI index (Dar and Dar 2021; Noorisameleh et al. 2021; Salehnia et al. 2017). Limited by the number of meteorological stations, the study selected SPI as the index to confirm the droughts and floods grade.

Previous studies of climate tendency generally focused on time series analysis (Zhao et al. 2019). In reality, different meteorological data often have different distribution functions. Therefore, many researchers use non-parametric method to study the trend of time series and other factors. Sen's slope combined with Mann–Kendall trend test are the commonly used tools for detecting the trend value and significance of climate elements (Yilmaz and Tosunoglu 2019). In recent years, many signal processing methods have emerged. In view of the nonlinearity and high signal-to-noise ratio of time series, some denoising methods have been proposed one after another. Empirical mode decomposition (EMD) (Huang et al. 1998), as a method of adaptively processing data, has proven to be a very useful non-parametric signal denoising method (Gao and Shang 2019). It can adapt to the analysis of nonlinear and nonstationary signals. The EEMD is improved on the former; white noise interference is introduced, which avoids the problem of modal aliasing to a certain extent (Wu and Huang 2011). A few scholars have applied this signal processing method to climate research (Franzke 2012; Zhou et al. 2014). The climate system is a typical chaotic and nonlinear system. Correspondingly, meteorological data is also a nonlinear and nonstationary time series. For this kind of sequence, the EEMD is used to decompose it into different frequency modes (Chang and Liu 2011) and the possible change rules, and the physical mechanism of different modes can be found. On the spatial scale, the spatial changes of climate element trends in areas affected by humans have also attracted more and more

attention. As a dimensionality reduction method, EOF separates the time field and the space field to facilitate better identification of the spatial modalities of the elements and is widely used in meteorological research (Zveryaev 2006).

Meanwhile, hydrometeorological teleconnections play a vital role in hydrological processes (Shi et al. 2021), because it can reflect the influence of large-scale circulation on meteorological elements. Based on it, additional studies are required to understand the transformation mechanisms of drought and flood characteristics, especially their possible relationship with large-scale climate indices. Cross-wavelet transform is a new signal analysis technique. It is often used to study the correlation between two time series in time–frequency domain. Many scholars have carried out a large number of researches on the teleconnection of climate tendency and large-scale meteorological factors by this method (Liu et al. 2020; Voice and Hunt 1984). In the TLB, Yin et al. studied the relationship between flood and drought disasters and El Niño–Southern Oscillation (ENSO) from 1857 to 2003 based on EOF and XWT methods (Yin et al. 2009). Beyond that, there were no systematic study of the teleconnection between climate trends and large-scale climate factors in the TLB.

The Taihu Lake Basin (TLB) is one of the most important basins in China, which is located in the Yangtze River Delta. It is the most urbanized and economically developed region in China. Influenced by its subtropical monsoon climate and geographical location (Wang et al. 2020b), the basin has abundant rainfall and frequent flood disasters in the flood season. To effectively monitor and predict the occurrence of flood events and minimize extreme losses, many studies have been conducted on flood disasters in the TLB (Jiang et al. 2021; Luo et al. 2019). However, research on watershed drought is limited. Due to its topography and geographical location, among other reasons, the spatiotemporal distribution of precipitation in the TLB is uneven, resulting in the existence of drought in the basin. So, it is necessary to study the spatiotemporal distribution characteristics of drought and flood in the TLB. Previous studies on the characteristics of drought and flood mostly focused on a single scale of time series. Here, we used a new signal processing method (EEMD), which can more clearly analyze the multi-time scale oscillation and spatiotemporal characteristics of droughts and floods. For the study of teleconnection relationships, previous studies only consider the teleconnection patterns. On this basis, this article takes into account sunspots, a factor that has an important impact on climate change.

Few works have been conducted on the spatiotemporal distribution of droughts/floods and systematic study of teleconnection in the TLB. To fill this gap, three specific goals were identified: (1) investigate the multiscale oscillation characteristics and variation trends of drought and flood in

the TLB, (2) explore the heterogeneity in the spatial distribution of SPI trends and discover the main spatial modes that lead to such difference, and (3) understand the influence mechanism of large-scale climate indices on drought and floods and its predictability.

Study area and data

The TLB is located between 119°11′–121°53′ E and 30°28′–32°15′ N, as shown in Fig. 1. It has a subtropical monsoon climate, with an annual average temperature of 15.5 °C and an annual average rainfall of 1181 mm. The rainfall is distributed unevenly throughout the year, falling mainly from May to September, with a tremendous interannual variation. The Yangtze River bounds the basin in the north, Hangzhou Bay in the south, the East China Sea in the east, and Maoshan, Jieling, and Tianmu Mountains in the west. The total area of the basin is approximately 36900 km². The terrain is high in the west and low in the east, high around, and low in the middle, with a disk-like distribution. The entire basin is dominated by plains, which account for two-thirds of the total basin. The basin is characterized by

numerous lakes and a dense river network. The water surface area of the basin is 2338 km², and the water surface covers 17% of the whole basin. The river network density in the plain area is 3.2 km/km², which constitutes a typical “southern Jiangnan water network.”

Based on the consistency and integrity of the data, daily precipitation data from 63 hydrological stations with uniform distribution in the TLB for 54 years (1965 to 2018) were selected in this study. The data were obtained from the China Meteorological Service Network (<https://data.cma.cn/>), and the data were verified by the Hydrological Yearbook of the People’s Republic of China (1965 to 2018). Large-scale meteorological indices included the Arctic Oscillation (AO), Pacific Oscillation (PDO), Indian Ocean Dipole (IOD), North Atlantic Decadal Oscillation (AMO), and El Niño–Southern Oscillation, which came from the Earth System Research Laboratory (ESRL) of the US National Oceanic and Atmospheric Administration (NOAA) (<http://www.cpc.ncep.noaa.gov/>). The relative sunspot number came from the Data Centre of the Royal Belgian Observatory (<http://www.sidc.be/silso/datafiles>). The time span of the above large-scale meteorological indices was 1965–2018.

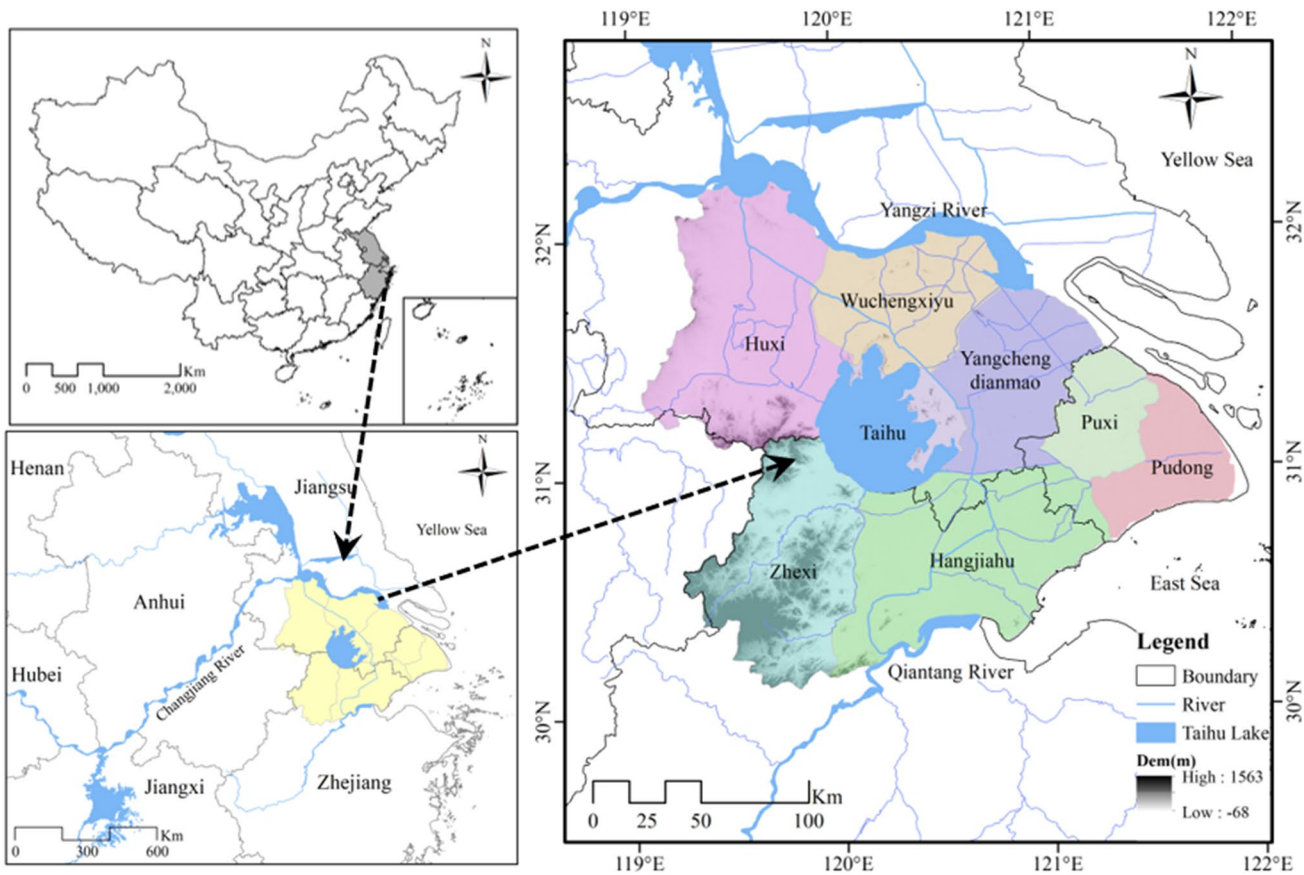


Fig. 1 Location of the study areas

Methodology

Standardized precipitation index (SPI)

The SPI applies to monitoring and assessing drought and flood conditions monthly and above. This index assumed that the precipitation complied with the γ distribution, and combined with the reality that the precipitation conforms to the skewness distribution, it can be obtained after standard normalization. We used 54 years (1965–2018) of monthly precipitation over the case study area for calculating it. The details of the SPI calculation were as follows:

- (1) Suppose the precipitation in a certain period of time is a random variable X , and its probability density function conforming to the Gamma distribution is

$$f(x) = \frac{1}{\beta^\gamma \Gamma(\gamma)} x^{\gamma-1} e^{-\frac{x}{\beta}} \tag{1}$$

where β and γ are size and shape parameters, respectively, which can be obtained by maximum likelihood estimate:

$$\beta = \frac{\bar{x}}{\hat{\gamma}} \tag{2}$$

$$\hat{\gamma} = \frac{1 + \sqrt{1 + 4A/3}}{4A}, \text{ with } A = \lg\bar{x} - \frac{1}{n} \sum_{i=1}^n \lg x_i \tag{3}$$

- (2) After the probability density function is determined, the probability that the random variable x is less than x_0 can be obtained for the precipitation x_0 in a certain year:

$$P(x < x_0) = \int_0^{x_0} f(x) dx \tag{4}$$

When the precipitation is 0, the event probability can be obtained by the following formula:

$$P(x = 0) = \frac{m}{n} \tag{5}$$

where m is the number of samples with precipitation of 0, n is the total number of samples.

- (3) By normalizing the distribution probability and performing an approximate solution, SPI can be obtained. The formula is as follows:

$$t = \sqrt{\ln \frac{1}{p^2}} \tag{6}$$

$$SPI = S \frac{t - (c2t + c1)t + c0}{((d3t + d2)t + d1)t + 1} \tag{7}$$

where P is the distribution probability of precipitation related to the Γ function, t is a function of P , and S is the positive and negative coefficient of probability density, which is related to P . When $P \leq 0.5$, then $S = 1$; when $P > 0.5$, sign reversal, and then $S = -1$, C_x and d_x are the calculation parameters of the approximate solution formula, and their values are as follows: $C_0 = 2.515517$, $C_1 = 0.802853$, $C_2 = 0.010328$, $D_1 = 1.432788$, $d_2 = 0.189269$, and $d_3 = 0.001308$. More details about the SPI computation can be found from the study of Mckee et al. (1993) and Dogan et al. (2012).

In this study, the SPI values at 3 and 12 months were used to represent the drought/flood characteristics of the basin at seasonal and annual scales, respectively. The seasons were generally divided meteorologically as follows: spring (March to May), summer (June to August), autumn (September to November), and winter (December to February). Therefore, the 3-month SPI of May, August, November, and February of the following year was used to represent the seasonal SPI of spring, summer, autumn, and winter, respectively, while the 12-month SPI of December for each year was defined as the annual SPI. For computing the SPI, a software tool was used from National Drought Mitigation Center (<https://droug.ht.unl.edu/monitoring/SPI.aspx>).

Drought and flood types are divided into 9 grades based on SPI, and the classification of grades is shown in Table 1.

Ensemble empirical mode decomposition

The EEMD method used in this paper introduced Gaussian white noise perturbation based on EMD and performed ensemble averaging which avoided the problem of modal mixing to some extent (Wu and Huang 2011). The original data sequence is reconstructed as multiple waves of a single frequency and a residual wave, the form is as follows:

$$x(t) = \sum_{i=1}^n IMF_i(t) + Res(t) \tag{8}$$

where i is the number of IMFs, $IMF_i(t)$ is the i^{th} IMF of the original data, $Res(t)$ is the residual term, and $x(t)$ is the SPI series on annual and seasonal scales. Each IMF reveals the

Table 1 Classification of grades of drought and wet for SPI

| Classification | SPI values | Classification | SPI values |
|------------------|-----------------------|----------------|--------------------|
| Extreme drought | $SPI \leq -2.0$ | Extreme flood | $SPI > 2.0$ |
| Severe drought | $-2 < SPI \leq -1.5$ | Severe flood | $1.5 < SPI \leq 2$ |
| Moderate drought | $-1.5 < SPI \leq -1$ | Moderate flood | $1 < SPI \leq 1.5$ |
| Mild drought | $-1 < SPI \leq -0.5$ | Mild flood | $0.5 < SPI \leq 1$ |
| Normal | $-0.5 < SPI \leq 0.5$ | | |

oscillation characteristics of the original data series on different characteristic time scales, while *Res* is an extremely low frequency wave, which can be regarded as a trend line to reveal the change trend of the original data series.

In this paper, EEMD decomposition of SPI-3 and SPI-12 was carried out to analyze the multi-time scale characteristics of drought/flood evolution in the basin. In addition, the significance test is performed by the set disturbance of white noise; the specific calculation steps are as follows:

$$\bar{T}_k = \frac{N}{NP_k} \tag{9}$$

$$E_k = \frac{1}{N} \sum_{i=1}^N |I_k(i)|^2 \tag{10}$$

where \bar{T}_k represents the average period of the k^{th} IMF, N represents the length of IMF sequence, NP_k is the peak number of IMF, E_k represents the energy density of the k^{th} IMF, and $I_k(i)$ represents the k^{th} IMF to be tested with white noise by Monte Carlo method.

For the k^{th} IMF with white noise added, the average of energy spectral density \bar{E}_k and the average period \bar{T}_k have the following relationship:

$$\ln \bar{E}_k + \ln \left\{ \bar{T}_k \right\}_\alpha = 0 \tag{11}$$

where α is the significance level.

Theoretically, the IMF of the white noise should be distributed on the line with the slope of -1 on the X -axis and Y -axis, but there is a deviation in practical application. Therefore, the confidence interval of the energy spectrum distribution of the white noise can be given as follows:

$$\ln \bar{E}_k = -\ln \left\{ \bar{T}_k \right\}_\alpha \pm \alpha \sqrt{2/N} e^{\ln(|\bar{T}_k|_{\alpha/2})} \tag{12}$$

At the specified significance level, the energy distribution of IMF is above the confidence curve, indicating that the significance test is passed; that is, the actual physical significance is included in the selected confidence level. On the contrary, it is considered that it has not passed the confidence test. All calculations in this section were implemented in MATLAB R2018a.

Empirical orthogonal function decomposition

Empirical orthogonal function decomposition was a method to analyze the data structure in the matrix and extract the primary data characteristic quantity (Lorenz 1956). It divides the meteorological field into two parts:

spatial patterns and temporal patterns. Therefore, it is also called space–time decomposition. The specific calculation processes are as follows:

- (1) For the preprocessed data, get the data matrix $X_{m \times n}$, take the cross product of X and its transpose, and get the square matrix $A_{m \times m}$:

$$A_{m \times m} = \frac{1}{n} X \times X^T \tag{13}$$

where m is the number of sites and n is the number of years.

- (2) The eigenvalue $(\lambda_1, \dots, \lambda_m)$ of the square matrix A and the eigenvector $V_{m \times m}$ are given as follows, and the principal components are calculated:

$$A_{m \times m} \times V_{m \times m} = V_{m \times m} \times P_{m \times m} \tag{14}$$

$$PC_{m \times n} = V_{m \times m}^T \times X_{m \times n} \tag{15}$$

where $P_{m \times m} = \text{diag}(\lambda_1, \dots, \lambda_m)$ and each row of data in PC corresponds to the time coefficient of each feature vector.

- (3) Calculate the explanatory rate of each mode to the total variance, and the variance can be simplified to be replaced by the characteristic root. The explanatory rate of the j^{th} mode to the total variance can be expressed as

$$\omega = \frac{\lambda_j}{\sum_{i=1}^m \lambda_i} \times 100\% \tag{16}$$

If the symbols of modal coefficients are the same, it indicates that the variation trend of regional elements is basically the same, and the high absolute value is located in the center. If the modal coefficient is positive and negative, it indicates that there are two distribution types of elements in the region. All calculations in this section were implemented in SPSS Statistics 24.

Cross-wavelet transform

Morlet wavelet has good time–frequency resolution, and its scale parameter is approximately equal to the Fourier period (Hao et al. 2012). Therefore, this study chose Morlet wavelet as the basis function, and its form can be expressed by the following formula:

$$\psi(t) = \pi^{-1/4} e^{\delta i t} e^{-t^2/2} \tag{17}$$

For the two known time series $x(t)$ and $y(t)$, the continuous wavelet transform coefficient of $x(t)$ is defined by the linear integral operator as

$$W^X(\alpha, \gamma) = \int_{-\infty}^{+\infty} X(t)\psi_{\alpha,\gamma}^*(t)dt = \frac{1}{\sqrt{a}} \int_{-\infty}^{+\infty} X(t)\psi_{\alpha,\gamma}^*\left(\frac{t-\gamma}{\alpha}\right)dt \tag{18}$$

with

$$\psi_{\alpha,\gamma} = \frac{1}{\sqrt{a}} \psi\left(\frac{t-\gamma}{\alpha}\right) \tag{19}$$

where α and γ are scale parameters and time shift parameters, respectively, $\psi_{\alpha,\gamma}$ is wavelet clusters generated by continuous translation or expansion of the mother wavelet $\psi(t)$, $W^X(\alpha, \gamma)$ is the wavelet coefficient of time signal $x(t)$, and $*$ represents the conjugate operator. Similarly, the wavelet coefficient $W^Y(\alpha, \gamma)$ of the time signal $y(t)$ can be obtained.

By analogy with Fourier cross-spectrum (Liu 1994), the cross-wavelet transform of two time series $x(t)$ and $y(t)$ is defined as:

$$W^{XY}(u) = W^X(u)W^{Y*}(u) \tag{20}$$

$$u = f(\alpha, \gamma) \tag{21}$$

where $W^X(u)$ is the wavelet coefficient of time series $x(t)$; $W^{Y*}(u)$ is the complex conjugate of the wavelet coefficients of $y(t)$; and u is the function related to α and γ . The power of the cross-wavelet transform is defined as $|W^{XY}(u)|$; the larger the value is, the two have the same high energy region, and the more significant the correlation between them is. The complex parameter $\arg(W^{XY})$ can be used to explain the local relative phase of $x(t)$ and $y(t)$ in the time–frequency domain.

In this paper, cross-wavelet based on Morlet wavelet is used to study the teleconnection; monthly data from 1965 to 2018 were used for both SPI and large-scale climate indices. This analysis was implemented by MATLAB R2018a. More

details on XWT can be obtained from the study of Torrence and Compo (1998) and Grinsted et al. (2004).

Climate propensity rate

A linear equation often expresses trends in climatic elements such as temperature or precipitation (Huang et al. 2021). In this study, Y represented the yearly scale SPI with sample size n , and t illustrated the corresponding time from 1965 to 2018. Establish a linear regression equation with one variable between Y and t , and the form is as follows:

$$Y = a_0t + a_1(t = 1, 2, 3, \dots n) \tag{22}$$

The coefficients in the equation can be obtained by ordinary least squares or empirical orthogonal polynomial, and 10 times of the regression coefficient a_0 is called the climate tendency rate.

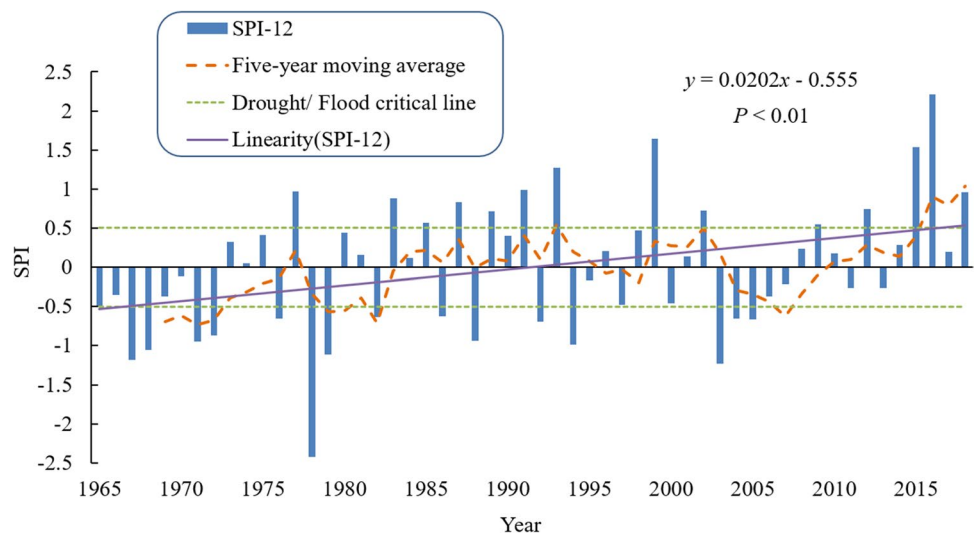
Result and discussion

Temporal characteristics of drought and flood

In this paper, the SPI–12 series was chosen to analyze the temporal variation characteristics of drought and flood in the TLB. The corresponding 5-year moving average and trend line were calculated based on the annual SPI of 54 years (1965 to 2018). The results are shown in Fig. 2.

It can be seen from the yearly SPI that the drought/flood index of the TLB in the last 54 years showed obvious oscillations, and the droughts alternated with the floods. Combined with the trend line, it can be found that the drought/flood index of the whole basin increased at a rate of 0.2 per decade ($P < 0.01$), indicating that TLB as a

Fig. 2 Annual SPI sequence of Taihu Lake Basin



whole developed in a humid direction. The periodic variation trend of the drought/flood index was obtained from the 5-year moving average curve. In 1977, 1982, 2002, and 2007, there was a clear turning point showing an “up-down-up-down-up” trend. Over the past 54 years, the entire river basin had two alternating stages of drought and flood, belonging to the flood stage at present. According to the analysis of each stage, the drought period was mainly concentrated in 1965–1982 and 2003–2007, with most of the years experiencing light drought. The SPI values in 1967, 1968, 1979, and 2003 were -1.19 , -1.06 , -1.11 , and -1.23 , respectively, indicating moderate drought. Severe drought was observed in 1978 when the SPI value reached -2.42 . Years of relative flooding were mainly concentrated in 1977, 1983–1993, 1999–2002, and 2012–2018, most of which were considered normal or light floods. In 1993, 1999, and 2015, moderate flood years occurred, with SPI values of 1.27 , 1.65 , and 1.54 , respectively. In 2016, the SPI reached 2.21 , which was an extreme flood year.

Consulted Yearbook of Meteorological Disasters in China (2004–2019) can find the year of corresponding drought (flood) records. In 1978, there was a national drought. In 2016, the Yangtze River Delta region was subjected to several heavy rainfall events and convection flows, indicating that the calculated annual SPI results were reasonable. Over the past 54 years, the TLB gradually developed in a humid direction, the occurrence frequency of drought events decreased, and the occurrence probability of flood events increased. Before 1979, the whole basin was in a primarily dry period; during the period spanning 1982–2002, it was in the dry–wet alternation period; and during the 2003–2006 range, it was in the second dry period. In recent years, the whole basin has been trending in a flooding direction.

Multi-time scale periodic oscillation characteristics

This study used the EEMD method to decompose the SPI series of 54 years from 1965 to 2018 to study the multi-time scale periodic oscillation characteristics of drought and flood changes. All decomposition results from the annual SPI series can be found in Fig. 3. IMFs (IMF1–4) are shown in Fig. 3a. In addition, each IMF was reconstructed interannually and interdecadally. The reconstructed results and the residual components (Res) are plotted together in Fig. 3b. Finally, the variance contribution rates of IMFs and Res to the original SPI series were calculated, and the oscillation period of each IMF was calculated. The calculation results can be found in Table 2.

As shown in Fig. 3a, each IMF decomposed from the annual SPI series reflects the fluctuation characteristics of different time scales from high frequency to low frequency. IMF₁ had the highest fluctuation frequency and amplitude. With increasing order numbers, the amplitude and frequency gradually decreased. At the same time, each IMF had a relatively stable quasiperiodicity. IMF1 and IMF2 had 2.92-year (quasi-3-year) and 6.3-year (quasi-6-year) mean periods at the interannual scale, respectively. IMF3 and IMF4 had 10.8-year (quasi-10-year) and 27-year mean periods at the interdecadal scale, respectively. According to the significance test results, only IMF₃ passed the 95% confidence interval test, indicating that within the 95% confidence interval, IMF₃ contained more information with actual physical significance, and other components contained less information.

As shown in Table 2, the variance contribution rate of the quasi-3-year period represented by IMF₁ was the largest, reaching 27.4%. The amplitude showed a “decrease-increase-decrease” trend. This was followed by IMF₂ (25.1%), IMF₃ (19.8%), and IMF₄ (17.2%). The interannual

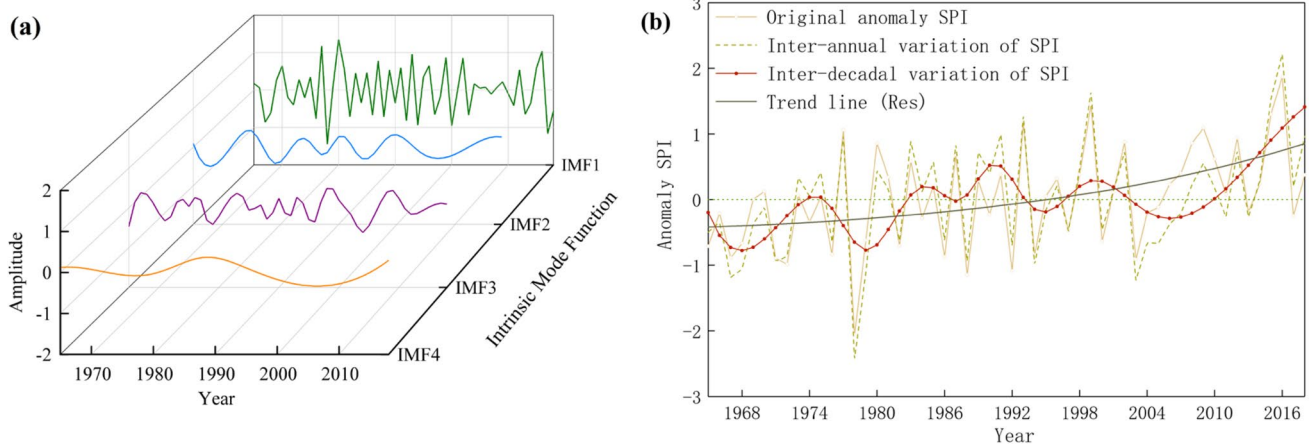


Fig. 3 Decomposition results of the annual SPI. **a** Four intrinsic mode functions (IMFs). **b** Comparison of interannual and interdecadal SPI changes with the original SPI anomaly

Table 2 Period and variance contribution of components of SPI series in TLB

| Time scale | Index | IMF1 | IMF2 | IMF3 | IMF4 | Res |
|------------|---------------------------|------|------|-------|------|------|
| Annual | Period (year) | 2.92 | 6.35 | 10.8 | 27 | |
| | Variance contribution (%) | 27.4 | 25.1 | 19.8 | 17.2 | 10.5 |
| Spring | Period (year) | 3 | 6 | 15.43 | 27 | |
| | Variance contribution (%) | 30.7 | 23.4 | 19.9 | 15 | 11 |
| Summer | Period (year) | 3.27 | 6 | 12 | 18 | |
| | Variance contribution (%) | 37.1 | 21.9 | 18.6 | 12.9 | 9.5 |
| Autumn | Period (year) | 3.09 | 7.71 | 21.6 | 36 | |
| | Variance contribution (%) | 30.5 | 24.9 | 20.1 | 17 | 7.5 |
| Winter | Period (year) | 3.09 | 6.35 | 15.43 | 27 | |
| | Variance contribution (%) | 24.9 | 23.2 | 20.3 | 18 | 13.6 |

scale component had a 52.5% variance contribution rate to the annual SPI variation, occupying a dominant position. As seen in Fig. 2b, the reconstructed interannual SPI variation trend was almost completely consistent with the original SPI anomaly variation trend, indicating that interannual oscillation played a dominant role in the SPI variation of the TLB. Reconstructed interdecadal variation can effectively describe the period characteristics of SPI variation; that is, before 2005, SPI was about to rise in volatility, while after 2005, SPI was in a stage of rapid rise, revealing the climate modal transformation in the TLB circa 2005. The SPI fluctuates alternately from the original positive/negative phases, and the mode dominated by the negative phase turns to the climate model with a significant positive phase. The trending term can reflect the overall variation trend of the SPI of TLB during 1965–2018. The residual of the annual SPI series of the TLB showed a nonlinear upward trend, and the rate of increase was increasing. This indicated that during 1965 to 2018, the basin experienced a stage from drought to flood, with the degree of the flood still increasing. This is basically consistent with the results described above.

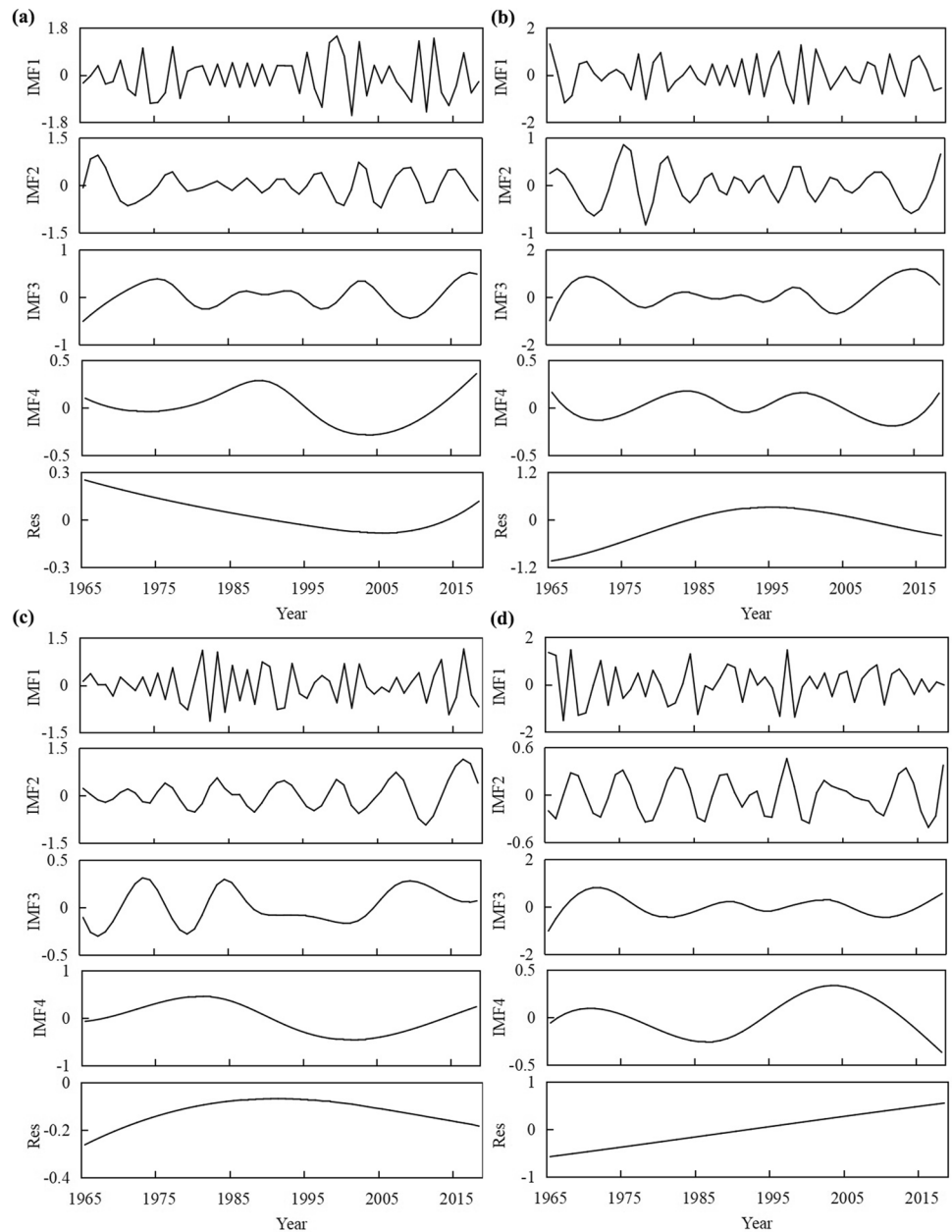
For each seasonal SPI series, the interannual scale IMFs (IMF_1 , IMF_2) had oscillation characteristics similar to those of the annual SPI series. However, each season's interdecadal scale components (IMF_3 and IMF_4) showed different oscillation characteristics from the annual SPI. For IMF_3 , as shown in Table 2 for all seasonal SPI series, the variance contribution rate of IMF_1 was the largest among all IMFs, reaching 30% except winter (24.19%). The second was IMF_2 , which contributed more than 20% of the variance. On the other hand, the contribution of IMF_3 and IMF_4 to the variance was relatively small. The variance contribution rate of the interannual scale IMFs (IMF_1 and IMF_2) in all seasons was more than 50% (except 48.1% in winter), larger than the interdecadal scale IMFs. This indicates that the interannual scale components (IMF_1 and IMF_2) in seasonal series were still the main components, and interannual oscillation played a dominant role in SPI variation. This was the same as with the annual SPI sequence.

To illustrate multiscale oscillation characteristics of the SPI, seasonal SPI sequences were also decomposed. The results of the seasonal SPI series are plotted in Fig. 4.

Spring Res showed a downward trend from 1965 to 2005, decreasing to the minimum value in 2005. It showed an upward trend, indicating that the TLB experienced a drought process in spring from 1965 to 2005 and then conducted a wet trend. However, in the past 54 years, the overall Res has shown a downward trend. This result showed that the basin was experiencing a drought in spring. The summer Res showed an upward trend during 1965–1995, reached an extreme value in 1995, and then showed a downward trend, indicating that the basin in summer experienced a wet process before 1995 and then developed in the drought direction. The overall Res showed an upward trend, indicating that the whole basin was experiencing a wet process in summer. The variation trend of Res in autumn was similar to that in summer, but the maximum value appeared in 1990. Before that, the basin experienced a process of wetting in autumn, which was followed by the trend of drought developing. At the same time, the Res still showed an upward trend, indicating that the basin had a wetting tendency in autumn. The variation trend of Res in winter showed a linear rising trend, indicating that the overall trend of winter in the TLB was wet during the study period.

Compared with previous studies, this study used an improved EEMD method, which can suppress the end effect and mode mixing in the decomposition process compared with the traditional EMD method. Previous research methods generally only considered the overall linear trend of drought and flood change, which often failed to reveal the phase trends of drought and flood variations. In contrast, the EEMD method performed better in this regard. The result indicated that the TLB showed a trend of wetting at the characteristic scales of year, summer, autumn, and winter and a trend of drying in spring. That is the same as the results of previous studies (Hu et al. 2021), which proved that the EEMD method was well used in the TLB. In addition, quasiperiodic oscillations with relatively stable drought

Fig. 4 The IMF and Res of the seasonal SPI in Taihu Lake Basin (TLB) from 1965 to 2018 by EEMD: **a** spring, **b** summer, **c** autumn, and **d** winter



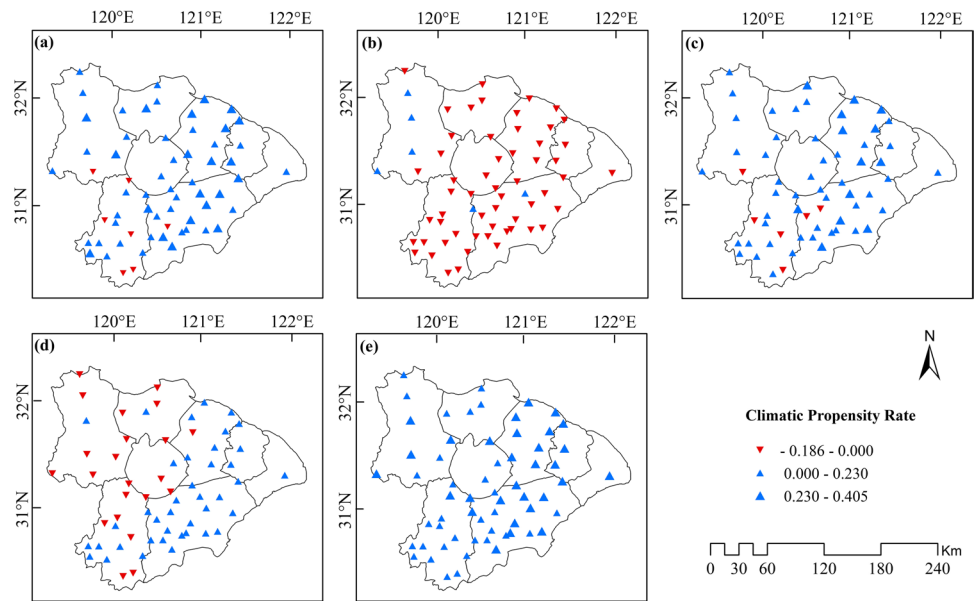
and flood characteristics in the TLB were also obtained by the EEMD method. It was observed that the SPI series in the TLB was a nonlinear and periodically oscillating process from 1965 to 2018; the annual SPI series had quasi-3-year (IMF_1) and quasi-6-year (IMF_2) oscillation periods on the interannual scale and quasi-10-year (IMF_3) and 27-year (IMF_4) oscillation periods on the interdecadal scale, respectively. The seasonal SPI series had similar periods to the annual SPI series on the interannual scale but differed on the interdecadal scale. Meanwhile, in both SPI series, interannual oscillation always played a more dominant role in the process of SPI variation than the interdecadal oscillation. The above results showed that EEMD, as a signal analysis

technique, has obvious advantages in dealing with nonlinear and nonstationary time series and can reflect the variations in drought and flood characteristics in the Taihu Lake Basin excellently.

Spatial distribution characteristics of drought and flood

The annual and seasonal SPI climate propensity rate distributions were plotted, and the results are shown in Fig. 5. The positive triangle indicates that the SPI tended to increase, and there was a tendency to become wetter; similarly, the inverted triangle indicates that there was a tendency towards

Fig. 5 Spatial distribution of SPI climate propensity rate in TLB during 1965–2018: **a** annual, **b** spring, **c** summer, **d** autumn, and **e** winter



drought at this location. To make it easier to distinguish, the positive triangle was divided into two levels of display according to the degree of tendency, with the larger triangle indicating a greater degree of tendency.

As seen from the annual SPI climate propensity rate distribution (Fig. 5a), save for the mountainous areas within the southern Zhexi sub-region, all other basin regions showed a trend from dry to wet ($P < 0.01$), with the most apparent trend in the Yangchengdianmao and Hangjiahu sub-regions. Fig. 5b to e show the spatial distribution of the SPI climate tendency in different seasons in the TLB. Most of the basin showed a significant drought trend in spring ($P < 0.05$), except for some localized areas in the Huxi sub-region. The spatial distribution of the propensity rate in summer was similar to that of the whole year, with the wetting centers mainly concentrated in the Yangchengdianmao and Hangjiahu sub-regions. The wetting trend gradually decreased from east to west, except for some areas in the mountainous areas of the Zhexi sub-region, and tended to become dry, and the whole basin had a tendency to become wet ($P < 0.01$). In autumn, the spatial distribution of the propensity rate was more complex, with a trend of wet to dry from east to west. The Yangchengdianmao and Hangjiahu sub-regions were still wet centers ($P < 0.01$), while the mountainous areas in the southern Zhexi sub-region also showed a non-significant wetting trend. The eastern and northeastern parts of the basin, including the Huxi sub-region and most of the Wuchengxiyu sub-regions, and the mountainous areas in the northern part of the Zhexi sub-region showed a non-significant drying trend. In winter, the whole basin showed a wetting trend ($P < 0.01$), and the degree of tendency was the highest among the four seasons, with no trend towards drought in the basin.

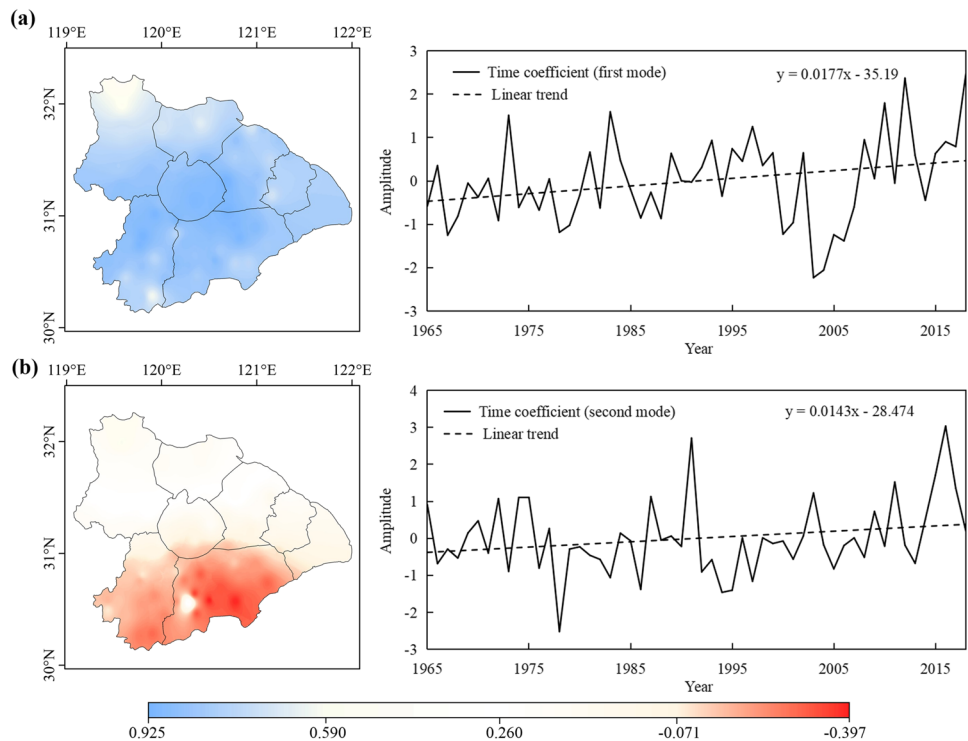
To better reflect the spatial distribution characteristics of drought and flood in the TLB, the EOF method decomposed the annual SPI series to obtain the main spatial distribution modes of drought and flood. Table 3 shows the first five eigenvalues and contribution rates of the decomposition of the annual SPI series. The cumulative contribution rate of the first five eigenvectors reached 86.77%, and the cumulative contribution rate of the first two eigenvectors was 78.48%. Therefore, the first two eigenvectors can explain the spatial distribution characteristics of drought and flood in the TLB in the past 54 years. The main spatial distribution modes of drought and flood in the TLB are shown in Fig. 6.

The variance contribution of the first mode eigenvector was 70.43%, which was much higher than that of the other modes and was the primary form of the spatial distribution of drought and flood variability in the TLB. As seen in Fig. 6a, the first spatial mode coefficients ranged from 0.57 to 0.93 and were positive across the basin, indicating that the spatial distribution of drought and flood changes was consistent during 1965–2018. In other words, the whole basin was either widespread drought or overall flood, which was

Table 3 Eigenvalues and contribution of EOF decomposition of annual SPI series of TLB

| Modal | Eigenvalue | Variance contribution/% | Cumulative variance contribution/% |
|-------|------------|-------------------------|------------------------------------|
| 1 | 43.67 | 70.43 | 70.43 |
| 2 | 2.99 | 8.05 | 78.48 |
| 3 | 2.52 | 4.05 | 82.54 |
| 4 | 1.47 | 2.36 | 84.90 |
| 5 | 1.15 | 1.85 | 86.76 |

Fig. 6 Eigenvector distribution and time coefficients of vector field: **a** the first mode and **b** the second mode



mainly the result of the influence of large-scale meteorological factors. However, the degree of drought (flood) varied from region to region. The high value centers were located in the central and western parts of the basin, including Taihu Lake, the northeastern Hangjiahu sub-region, the northern of Zhexi sub-region, and the south-eastern Yangchengdian-mao sub-region, indicating that these areas were the most sensitive and had the most obvious changes in drought and flood. Meanwhile, the northern Huxi and southern Zhexi sub-regions were the main areas of low values, indicating that the differences in these areas were less pronounced and that the influence of the first mode was more negligible. The temporal coefficients showed a significant ($P < 0.05$) upward trend over 54 years, indicating that the whole basin developed towards floods and alleviated the drought situation.

The variance contribution of the second mode eigenvector reached 8.05%, which was also the primary form of drought and flood distribution. As shown in Fig. 6b, the coefficients corresponding to this mode ranged from -0.39 to 0.6 , with positive centers occurring in the northern part of the basin, including the northern parts of Huxi and Wuchengxiyu sub-regions. Negative centers appeared in the southern part of the basin, mainly in the Hangjiahu sub-region, with an overall south-north reverse distribution, either, i.e., drought in the south and flooding in the north or flooding in the south or drought in the north at the same time. This was primarily the result of the influence of geographical location and topography. The time coefficients show a non-significant increasing trend over the past 54 years, with predominantly

negative values before 1990 and mostly positive values afterwards. This suggests that the TLB was characterized by drought in the north and flood in the south until 1990, after which the basin gradually changed to flood in the north and drought in the south.

As one of the most economically developed regions in China, the Taihu Lake Basin is also the region most affected by climate and is experiencing severe and frequent flooding periods. As one of the most studied basins in China, most studies have only considered aspects of the basin that suffer from flood disaster. Although drought is often neglected, the basin also faces a certain degree of influence of drought in different seasons due to topography and geographical location. This study analyzed the spatial and temporal variations in drought and flood characteristics in the TLB over the past 54 years and observed significant spatial and temporal heterogeneity using the SPI. At the same time, it made clear the drought-prone regions and flood-prone regions in the basin. The results can provide reference values for the basin's flood control and drought resistance works in the basin.

Correlation analysis of drought and flood changes with sunspots and large-scale meteorological factors

In this paper, the correlation between the SPI and several large-scale climate indices was investigated, and the trend lines of all indices save for sunspots were fitted by polynomials. The results are shown in Fig. 7.

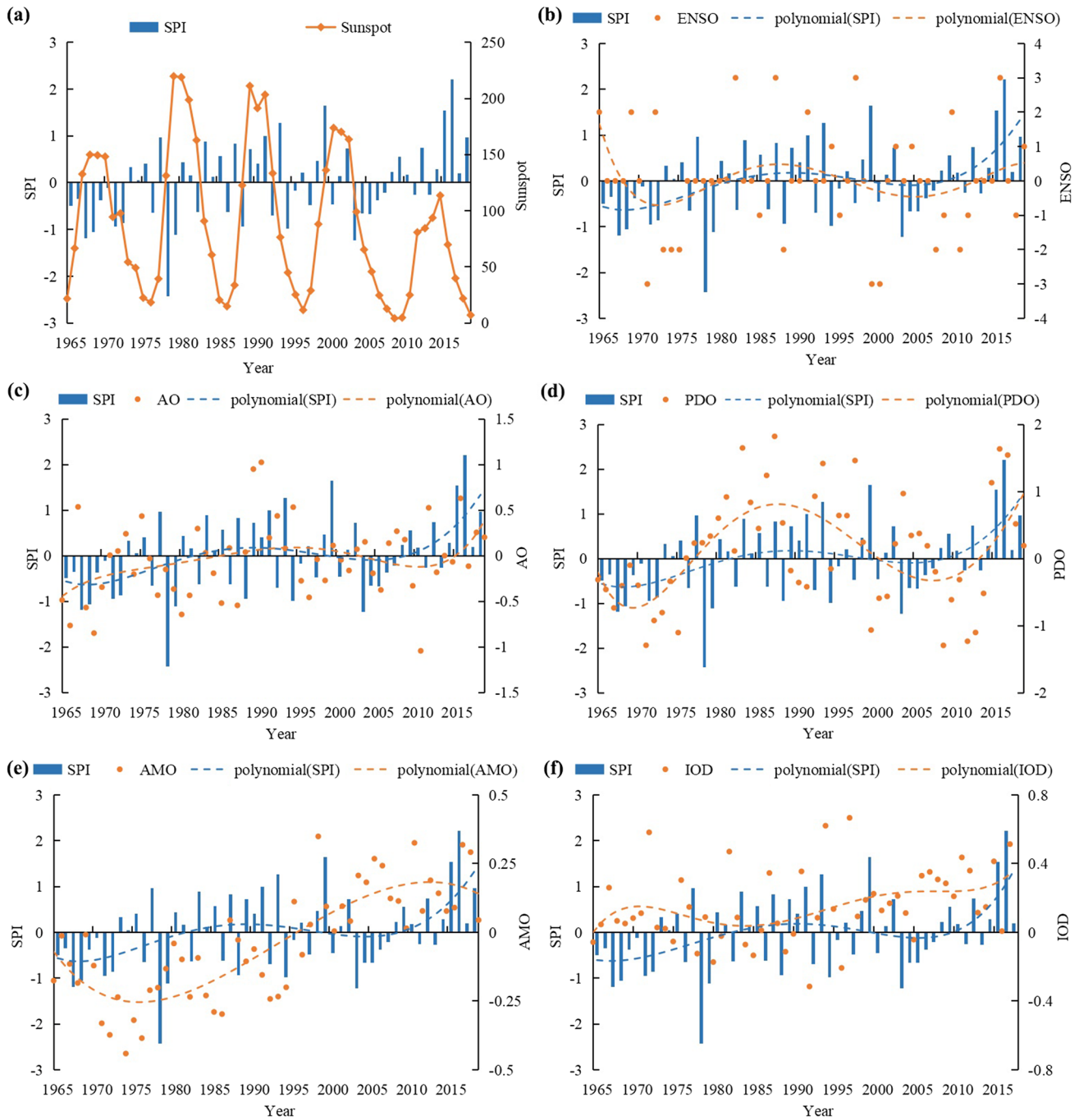


Fig. 7 Relationship between the variation trend of the SPI and large-scale climate indices: **a** sunspot; **b** ENSO; **c** Arctic Oscillation; **d** Pacific Decadal Oscillation; **e** Atlantic Multidecadal Oscillation; **f** Indian Ocean Dipole

As shown in Fig. 7a, during the 65 years (1965 to 2018), the relative sunspot number had five maximum years (1968, 1979, 1989, 2000, 2014) and six minimum years (1965, 1976, 1986, 1996, 2008, 2018), maintaining a quasiperiodic variation of 11a, which was consistent with the 10.8-year (quasi-11-year) oscillation period possessed by the annual SPI in the TLB on the interdecadal scale. There was a clear

negative correlation between the relative sunspot number and annual SPI. The higher the relative sunspot number, the lower the SPI and the drier the climate; the opposite was also found to be true. The extreme value of SPI was not synchronized with the extreme value of relative sunspot number, and there was often a lag. The results of the analysis of the frequency of drought and flood in the basin in the years

around the time of maximum (M) and minimum (m) sunspot values are shown in Table 4. During these years around the maximum sunspot, totaling 15 years, seven drought events (46.7%) and three flood events (20%) occurred, indicating that the frequency of drought events was greater than that of flood events before and after maximum sunspot year. Four drought events of medium drought and above occurred, and two flood events of medium flood and above occurred, accounting for 26.6% and 13.3% of the totaling 15 years. During the year before, during, and after the minimum sunspot (a total of 16 years), two drought events (12.5%) and five flood events (31.3%) occurred, indicating that the frequency of flood events was greater than that of drought events before and after the minimum sunspot year. During these periods, there were no drought events of medium drought and above (0% of the total) and two flood events of medium flood and above (12.5% of the total). On the other hand, there were 30 drought and flood events in 54 years (1965 to 2018), including 16 droughts and 14 floods, of which 5 years had moderate droughts and above, accounting for 9.3% of 54 years, and 4 years had moderate floods and above, accounting for 7.4% of 54 years. This indicates that extreme events occurred much more frequently in the vicinity of extreme sunspot years than in other years, providing a theoretical basis for strengthening the prediction prevention and control of extreme events.

Fig. 7 b to f show the correlation between the SPI and various atmospheric circulation indices. From Fig. 7b, it can be seen that in the 54 years from 1965 to 2018, seven strong ENSO events occurred, including four El Niño events and three La Niña events. When the ENSO intensity was positive, the SPI values were mostly positive, indicating that when warm events occurred, the precipitation increased and tended to be flooded. Conversely, when cold events occurred, the SPI values were mostly negative, and the basin tended towards drought. From the trend lines of both, it can be found that the changes in ENSO intensity and SPI were not synchronous, and most extreme drought and flood events tended to occur within 1–3 years after the occurrence of strong ENSO events, indicating that there was a certain lag between the two, but the correlation was not clear.

As shown in Fig. 7c, the SPI index was positively correlated with the AO index. This was because when the AO

intensity was high, the temperature in the middle and high latitudes of China was high, while precipitation increased and the basin developed in the direction of wetness; when its intensity was low, the temperature was low, precipitation decreased, and the basin became dry. Figure 7d shows that there was a significant positive correlation between the SPI index and the PDO index in the TLB. The two trend lines changed in the same way. That is, when the PDO was in a warm phase, the basin was prone to flood events, and when the PDO was in a cold phase, the basin was prone to drought events; the greater the absolute value of its intensity was, the greater the intensity of extreme drought and flood events. The positive and negative phase shifts experienced by the PDO in 1976 and 2002 corresponded to the drought and flood shifts in 1980 and 2010 in the TLB, which proved that there was a lag between the two. Figure 7e shows the negative correlation between the SPI index and AMO index. In 1975–2010, the AMO exhibited an upward trend, the SPI index exhibited a downward trend, and the basin developed towards drought. After this, the AMO exhibited a downward trend, the SPI index was upward, and the basin developed towards flooding. The two extreme drought and flood events in the basin (1978 drought and 2016 flood) occurred several years after the extreme values of AMO, indicating that there was a hysteresis between the two. Figure 7f shows a negative correlation between the SPI index and the IOD index. The IOD was positive in most years, and when the IOD index increased, the basin tended to experience drought.

Analysis of driving forces of drought and flood variation in Taihu Lake Basin

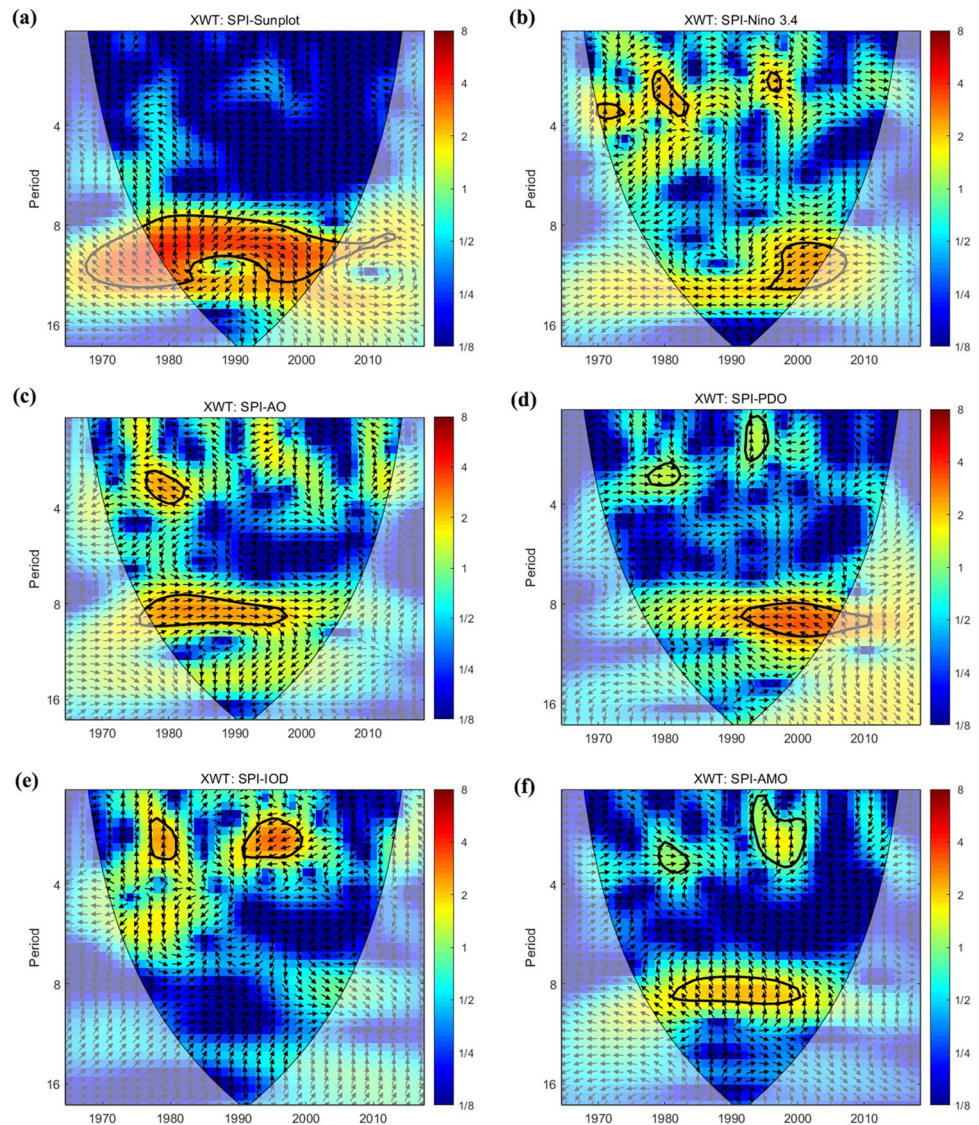
The XWT can highlight the common frequency and phase relationship between the two series in time–frequency space, which was used to draw the cross-wavelet power spectrum between the SPI and various large-scale meteorological factors (Fig. 8). The thin black line was the cone of influence, with effective spectral regions within it. The thin black contours represented the significant region with a 5% significance level by the red noise test. The color of the power spectrum ranged from blue to red, and a darker color indicated a higher energy density. The relative phase between the SPI and the large-scale climate indices is indicated by

Table 4 Statistics of drought and flood near sunspot extreme year in the TLB

| Level | m – 1 | m | m + 1 | Sum | M – 1 | M | M + 1 | Sum |
|----------------------------|-------|---|-------|-----|-------|---|-------|-----|
| Moderate drought and above | 0 | 0 | 0 | 0 | 2 | 2 | 0 | 4 |
| Mild drought | 0 | 1 | 1 | 2 | 1 | 1 | 1 | 3 |
| Normal | 4 | 3 | 2 | 9 | 1 | 1 | 3 | 5 |
| Mild flood | 1 | 1 | 1 | 3 | 0 | 1 | 0 | 1 |
| Moderate flood and above | 0 | 1 | 1 | 2 | 1 | 0 | 1 | 2 |

M, maximum sunspot year, m, minimum sunspot year

Fig. 8 XWT of SPI with sunspots and atmospheric circulation: **a** SPI sunspots, **b** SPI-El Niño–Southern Oscillation, **c** SPI-Arctic Oscillation, **d** SPI-Pacific Decadal Oscillation, **e** SPI-Indian Ocean Dipole, **f** SPI-Atlantic Multidecadal Oscillation



arrows, the arrow to the right (left) indicates in-phase (anti-phase), and up (down) indicates that the meteorological indices were in-phase ahead (lagging) of the SPI.

Figure 8a shows the XWT of the SPI and sunspots. There was a statistically significant relationship between sunspots and the SPI index in an 8- to 12-year period, mainly from 1975 to 2005. The arrows in the cross-spectrum point to the right indicate an in-phase relationship between the two in time and frequency. The arrows point to the upper right from 1975 to 1990, indicating that the SPI lagged the sunspots by 1–1.5 months, a phase difference of 30–45°. From 1990 to 2005, it began to point to the lower left, indicating that although the energy of the two series of cross-wavelets passed the red noise test, it did not form a stable relationship.

The XWT of the SPI and Niño 3.4 in Fig. 8b shows significant typical power in the 3–4-year band from 1970 to 1975, with the arrows pointing straight up, indicating that

Niño 3.4 led the SPI by 90°, which meant a lag between the SPI and Niño 3.4 variations. There was also a 1–4-year band from 1980 to 1985, with the arrows pointed right up, indicating an in-phase relationship. The phase angles were between 45° and 60°, which meant that the SPI lagged Niño 3.4 by 1.5–2 months. In addition, there was 2–3-year band from 1996 to 1998. The arrows pointed to the left, indicating that the SPI and Niño 3.4 showed an anti-phase relationship during this period. Still the maintenance time was short, and a stable correlation could not be formed. There were also 8–14-year bands at higher time scales, concentrated in 1995–2010, with the arrows pointing to the lower left, indicating a negative phase between the SPI and Niño 3.4. The average phase angle was 30–45°, indicating that the variations in the SPI value were 1–1.5 months ahead of the variations in Niño 3.4.

The XWT of the SPI and AO (Fig. 8c) shows that the SPI and AO had significant common power in the 3–4-year band from 1977 to 1983, with the arrows pointed to the upper left and the average phase angle difference of 30–45°, which indicated that the SPI and AO were in an anti-phase relationship and AO activity was 1–1.5 months ahead of the SPI change at this scale. In addition, another significant common power was still observed in the 8–10-year band in the high-frequency region. This was concentrated in 1975–2000, with the arrows pointed to the right, indicating an in-phase relationship between the SPI and AO.

Figure 8d shows the XWT of the SPI and PDO. From the above figure, it can be seen that the SPI and PDO showed significant common power in the 2–4-year band from 1975 to 1985, in the 1–3-year band from 1990 to 1998, and in the 8–12-year band from 1990 to 2010. Higher common powers were observed in the high time scale band than in the low time scale band. In the 2–4-year band, arrows pointed to the right, indicating an obvious in-phase relationship between the SPI and PDO, which meant that they changed in the same direction. In the 1–3-year band, arrows pointed straight up, which indicated that the phase of the PDO was 90° ahead of the SPI during this period. At higher time scales (> 8 years), arrows pointed to the upper left, and the mean phase angle was 30–45°, which indicated that the SPI lagged the PDO by 1–1.5 months.

Figure 8e shows the XWT of the SPI and IOD. There were two significant common power zones in which the SPI and IOD were shared with the 2–4-year band from 1975–1982 and 1990–2000. The two zones were not consistent; in the 2–4-year band of 1975–1982, the arrow pointed straight up, implying that IOD led the SPI by 90°, which meant that the SPI lagged approximately 3 months behind the IOD. Meanwhile, the common powers were higher in the 2–4-year band from 1990 to 2000. In this region, arrows pointed to the lower left, and the phase angle was 30–45° ahead, implying that the SPI and IOD were in an anti-phase relationship, while the change in SPI was ahead of the IOD by 1–1.5 months.

From the XWT of the SPI and AMO (Fig. 8f), the power spectrum energy of the two series was mainly concentrated in the cycles of 3–4-year (1980–2000), 0–4-year (1993–2005), and 8–10-year (1990–1995). The common energy frequency was lower on the two lower time scales (0–4-year and 3–4-year). The arrows pointed to the right in the 3–4-year cycle from 1980 to 1985, which meant that the SPI was in-phase with AMO during this period. In the 0–4-year cycle from 1993 to 2005, the arrows pointed straight up, indicating that the phase difference between the two was 90°. As the time scale increased, in the 8–10-year cycle from 1990 to 1995, arrows pointed to the upper left, with an average phase angle of 45–60°. This revealed an

anti-phase relationship between the SPI and AMO, while the SPI lagged the AMO by 1.5–2 months.

The TLB is in the lower reaches of the Yangtze River basin with a typical subtropical monsoon climate influenced by a variety of atmospheric circulations. Previous studies often only considered the correlation between atmospheric circulation and drought/flood indices, while sunspots, as an important factor of climate change on a global scale, were also included in this study. In terms of the degree of influence on the variations in SPI, sunspots were dominant, and they maintained a very high common frequency with SPI throughout the study period, which affected the global climate by influencing temperature and atmospheric circulation. In addition, with respect to the atmospheric circulation, the SPI was mainly negatively correlated with IOD, PDO, and Niño 3.4 and positively correlated with AO and AMO, all had different scale resonance cycles. Since the twenty first century, the main large-scale climate indices affecting the SPI in the TLB have changed from sunspots, AO, and IOD to sunspots, PDO, and Niño 3.4. In general, the SPI in the TLB was temporally correlated with all the above mentioned large-scale meteorological indices during the study period but was also divergent. Using ENSO as an example, this paper expressed the strength of ENSO events through Niño 3.4, which had an important influence on the variation in drought and flood characteristics in the TLB as the main air–sea interaction phenomenon in the eastern Pacific. When the ENSO warm event (El Niño) occurred, precipitation increased, and the basin evolved towards wetness. When the ENSO cold event (La Niña) occurred, precipitation decreased, which may lead to drought, and ENSO was positively correlated with the SPI in the TLB, which was consistent with the results of previous studies (Yin et al. 2009). There were also different correlations between other indices and the SPI. This part of the paper can provide a better understanding of the response relationships between drought and flood characteristics and various large-scale climate indices in the TLB to prevent and warn against possible extreme drought and flood events.

Conclusion

In this study, the spatiotemporal variation characteristics of drought and flood in the TLB for a total of 54 years from 1965 to 2018 were analyzed through the use of the EEMD method, EOF method, and climate propensity rate index, with SPI as a quantitative indicator. In addition, the relationship between the SPI and large-scale climate indices in the TLB was investigated by the cross-wavelet transform method to explore the response relationship between drought and flood variations characteristics and each climate indices. The main conclusions are as follows:

- (1) The yearly scale SPI showed a relatively stable quasi-periodic oscillation, and the overall trend is to become flood. The interannual variation played a dominant role in drought and flood variation in the TLB, the sum contribution rate of the interannual scale components reached 52.5%, verifying this view. This was also true at the seasonal scale.
- (2) Over the past 54 years, the TLB gradually developed from drought to flood at the annual and seasonal scales. Except for spring, which tended to become progressively drought. The variation trends of different regions in the basin were different. There were two modes of drought and flood in the TLB. The first mode was consistent across the basin, and the high value center was located in the Hangjiahu sub-region. The second was the south-north inverse distribution, with a high value center in the northern part of the basin and a low value center in the southern part.
- (3) Extreme drought and flood events were likely to occur near the extreme point of the relative sunspot number affected by solar activity. While there was a resonance period of 8–12a between the SPI and relative sunspot number, the two have been positively correlated for the past 54 years. In addition to the dominant influence of sunspots on the SPI, there were also correlations between the SPI and various atmospheric circulations. The SPI was mainly negatively correlated with IOD, PDO, and Niño 3.4 and positively correlated with AO and AMO, although there was still obvious heterogeneity in the strength of the correlation between various atmospheric circulations and the SPI.

On the basis of the traditional method to make improvements, the spatiotemporal characteristics of drought and floods in the TLB were studied at the same time. This provides a practical basis and guidance for flood and drought prevention in the TLB while analyzing their teleconnections with large-scale meteorological factors to clarify the influence mechanism of climate change on the droughts and floods to provide references for the effective utilization of water resources. It should be pointed out that only the role of natural factors was considered in the analysis of the causes of drought and flood characteristics in the TLB, but the mechanism of drought and flood events was very complex. As one of the fastest growing urbanized areas in China, the influence of human activities on drought and flood variations cannot be ignored. In subsequent studies, the combination of human activities and natural factors should be considered to analyze their response relationships to the drought and flood variation characteristics of the Taihu Lake Basin in an integrated manner.

Author contribution All authors have made a significant contribution to this research. Dingkui Wang and Feiqing Jiang conceived the research idea. Shengnan Zhu researched the corresponding methods. Dingkui Wang drafted the manuscript. Zengchuan Dong revised the paper. Zihan Ling edited the manuscript and processed the data. Jiayi Ma collected the data for analysis. All authors read and approved the final manuscript.

Funding This research was funded by the National Key Research and Development Program of China, grant number 2018YFC1508200.

Data Availability Not applicable.

Declarations

Ethics approval and consent to participate Not applicable.

Consent for publication Not applicable.

Conflict of interest The authors declare no competing interests.

References

- AghaKouchak A, Hoerling M, Feldman D, Huxman T, Lund J (2015) Water and climate: recognize anthropogenic drought. *Nature* 524:409–411
- Arduino G, Reggiani P, Todini E (2005) Recent advances in flood forecasting and flood risk assessment. *Hydrol Earth Syst Sci* 9:280–284. <https://doi.org/10.5194/hess-9-280-2005>
- Byun HR, Kim DW (2010) Comparing the effective drought index and the standardized precipitation index. *Options Méditerranéennes Séries A Mediterranean Seminars*
- Byun HR, Wilhite DA (1999) Objective quantification of drought severity and duration. *J Clim* 12:2747–2756. [https://doi.org/10.1175/1520-0442\(1999\)012<2747:OQODSA>2.0.CO;2](https://doi.org/10.1175/1520-0442(1999)012<2747:OQODSA>2.0.CO;2)
- Chang K-M, Liu S-H (2011) Gaussian noise filtering from ECG by wiener filter and ensemble empirical mode decomposition. *J Signal Process Syst Signal Image Video Technol* 64:249–264. <https://doi.org/10.1007/s11265-009-0447-z>
- Dar J, Dar AQ (2021) Spatio-temporal variability of meteorological drought over India with footprints on agricultural production. *Environ Sci Pollut Res*. <https://doi.org/10.1007/s11356-021-14866-7>
- Dogan S, Berktaç A, Singh VP (2012) Comparison of multi-monthly rainfall-based drought severity indices, with application to semi-arid Konya closed basin, Turkey. *J Hydrol* 470:255–268. <https://doi.org/10.1016/j.jhydrol.2012.09.003>
- Franzke C (2012) Nonlinear trends, long-range dependence, and climate noise properties of surface temperature. *J Clim* 25:4172–4183. <https://doi.org/10.1175/JCLI-D-11-00293.1>
- Gao J, Shang P (2019) Analysis of complex time series based on EMD energy entropy plane. *Nonlinear Dyn* 96:465–482. <https://doi.org/10.1007/s11071-019-04800-5>
- Grinsted A, Moore JC, Jevrejeva S (2004) Application of the cross wavelet transform and wavelet coherence to geophysical time series. *Nonlinear Process Geophys* 11:561–566. <https://doi.org/10.5194/npg-11-561-2004>
- Guttman NB (1999) Accepting the standardized precipitation index: a calculation algorithm. *J Am Water Resour Assoc* 35:311–322
- Hao Y, Liu G, Li H, Li Z, Zhao J, Yeh TJ (2012) Investigation of karstic hydrological processes of Niangziguan Springs (North China) using wavelet analysis. *Hydrol Process* 26:3062–3069

- Hayes MJ, Svoboda M, Wilhite DA, Vanyarkho OV (1999) Monitoring the 1996 drought using the standardized precipitation index. *Bull Am Meteorol Soc* 80:429–438. [https://doi.org/10.1175/1520-0477\(1999\)080<0429:MTDUTS>2.0.CO;2](https://doi.org/10.1175/1520-0477(1999)080<0429:MTDUTS>2.0.CO;2)
- Hu J, Liu Y, Sang YF, Liu C, Singh VP (2021) Precipitation variability and its response to urbanization in the Taihu Lake Basin, China. *Theor Appl Climatol* 144:1205–1218. <https://doi.org/10.1007/s00704-021-03597-x>
- Huang NE, Shen Z, Long SR, Wu MLC, Shih HH, Zheng QN, Yen NC, Tung CC, Liu HH (1998) The empirical mode decomposition and the Hilbert spectrum for nonlinear and non-stationary time series analysis. *Proc R Soc A-Math Phys Eng Sci* 454:903–995. <https://doi.org/10.1098/rspa.1998.0193>
- Huang X, Ma L, Liu T, Sun B, Chen Y, Qiao Z, Liang L (2021) Response relationship between the abrupt temperature change-climate warming hiatus and changes in influencing factors in China. *Int J Climatol* 41:5178–5200. <https://doi.org/10.1002/joc.7123>
- Hui T, Borth H, Fraedrich K, Su B, Zhu X (2014) Drought and wetness variability in the Tarim River Basin and connection to large-scale atmospheric circulation. *Int J Climatol* 34:2678–2684
- IPCC (2021) *Climate change 2021: the physical science basis*. Cambridge University Press, London
- Jiang F, Dong Z, Luo Y, Liu M, Zhu Z (2021) Response of flood events to extreme precipitation: two case studies in Taihu Basin, China. *Water Supply* 21:1629–1648. <https://doi.org/10.2166/ws.2021.001>
- Khan I, Lei H, Shah AA, Khan I, Muhammad I (2021) Climate change impact assessment, flood management, and mitigation strategies in Pakistan for sustainable future. *Environ Sci Pollut Res* 28:29720–29731. <https://doi.org/10.1007/s11356-021-12801-4>
- Li X, Sha J, Wang ZL (2019) Comparison of drought indices in the analysis of spatial and temporal changes of climatic drought events in a basin. *Environ Sci Pollut Res* 26:10695–10707. <https://doi.org/10.1007/s11356-019-04529-z>
- Liu PC (1994) Wavelet spectrum analysis and ocean wind waves. *Wavelets Geophysics* 4:151–166
- Liu W, Zhu S, Huang Y, Wan Y, Wu B, Liu L (2020) Spatiotemporal variations of drought and their teleconnections with large-scale climate indices over the Poyang Lake Basin, China. *Sustainability* 12:3526. <https://doi.org/10.3390/su12093526>
- Lorenz EN (1956) Empirical orthogonal functions and statistical weather prediction. *sci rep*.
- Luo Y, Dong Z, Guan X, Liu Y (2019) Flood risk analysis of different climatic phenomena during flood season based on copula-based Bayesian network method: a case study of Taihu Basin, China. *Water* 11:1534. <https://doi.org/10.3390/w11081534>
- Mckee TB, Doesken NJ, Kleist J (1993) The relationship of drought frequency and duration to time scales. In: 8th Conference on Applied Climatology American Meteorological Society, Anaheim.
- Noorisameleh Z, Gough WA, Mirza M (2021) Persistence and spatial-temporal variability of drought severity in Iran. *Environ Sci Pollut Res* 28:48808–48822. <https://doi.org/10.1007/s11356-021-14100-4>
- Palmer WC (1965) *Meteorological drought*. US Department of Commerce Weather Bureau Research paper.
- Paulo A, Martins D, Pereira LS (2016) Influence of precipitation changes on the SPI and related drought severity. An analysis using long-term data series. *Water Resour Manag* 30:5737–5757. <https://doi.org/10.1007/s11269-016-1388-5>
- Pei Z, Fang S, Wang L, Yang W (2020) Comparative analysis of drought indicated by the SPI and SPEI at various timescales in Inner Mongolia, China. *Water* 12:1925. <https://doi.org/10.3390/w12071925>
- Philip S, Kew SF, Van Oldenborgh GJ, Otto F, O'Keefe S, Haustein K, King A, Zegeye A, Eshetu Z, Hailemariam K (2017) Attribution analysis of the Ethiopian drought of 2015. *J Clim* 31:2465–2486. <https://doi.org/10.1175/JCLI-D-17-0274.1>
- Salehnia N, Ahn J (2022) Modelling and reconstructing tree ring growth index with climate variables through artificial intelligence and statistical methods. *Ecol Indic* 134:108496. <https://doi.org/10.1016/j.ecolind.2021.108496>
- Salehnia N, Alizadeh A, Sanaeinejad H, Bannayan M, Zarrin A, Hoogenboom G (2017) Estimation of meteorological drought indices based on AgMERRA precipitation data and station-observed precipitation data. *J Arid Land* 9:797–809. <https://doi.org/10.1007/s40333-017-0070-y>
- Salehnia N, Salehnia N, Torshizi AS, Kolsoumi S (2020) Rainfed wheat (*Triticum aestivum* L.) yield prediction using economical, meteorological, and drought indicators through pooled panel data and statistical downscaling. *Ecol Indic* 111:105991. <https://doi.org/10.1016/j.ecolind.2019.105991>
- Shi X, Huang Q, Li K (2021) Decomposition-based teleconnection between monthly streamflow and global climatic oscillation. *J Hydrol* 602:126651. <https://doi.org/10.1016/j.jhydrol.2021.126651>
- Torrence C, Compo GP (1998) A practical guide to wavelet analysis. *Bull Am Meteorol Soc* 79:61–78. [https://doi.org/10.1175/1520-0477\(1998\)079<0061:APGTWA>2.0.CO;2](https://doi.org/10.1175/1520-0477(1998)079<0061:APGTWA>2.0.CO;2)
- Vasileios M, Fabio F, Celine D, Iban A, Marco P, Luca M, Abdou A, Cesar CM (2018) Assessing floods and droughts in the Mékrou River Basin (WestAfrica): a combined household survey and climatic trends analysis approach. *Nat Hazards Earth Syst Sci* 18:1279–1296. <https://doi.org/10.5194/nhess-2017-195>
- Vicente-Serrano SM, Beguería S, López-Moreno J (2010) A multi-scalar drought index sensitive to global warming: the standardized precipitation evapotranspiration index. *J Clim* 23:1696–1718. <https://doi.org/10.1175/2009JCLI2909.1>
- Voice ME, Hunt BG (1984) A study of the dynamics of drought initiation using a global general circulation model. *J Geophys Res-Atmos* 89:9504–9520
- Wang X, Zhuo L, Li C, Engel BA, Sun S, Wang Y (2020a) Temporal and spatial evolution trends of drought in northern Shaanxi of China: 1960–2100. *Theor Appl Climatol* 139:981–982. <https://doi.org/10.1007/s00704-019-03069-3>
- Wang Y, Xu Y, Song S, Wang J, Zhang J (2020b) Assessing the impacts of climatic and anthropogenic factors on water level variation in the Taihu Plain based on non-stationary statistical models. *Environ Sci Pollut Res* 27:22829–22842. <https://doi.org/10.1007/s11356-020-08889-9>
- Wells N, Goddard S, Hayes MJ (2004) A self-calibrating palmer drought severity index. *J Clim* 17:2335–2351. [https://doi.org/10.1175/1520-0442\(2004\)017<2335:ASPDSI>2.0.CO;2](https://doi.org/10.1175/1520-0442(2004)017<2335:ASPDSI>2.0.CO;2)
- Wu Z, Huang NE (2011) Ensemble empirical mode decomposition: a noise-assisted data analysis method. *Adv Adapt Data Anal* 1:1–41
- Yang Q, Scanlon BR (2019) How much water can be captured from flood flows to store in depleted aquifers for mitigating floods and droughts? A case study from Texas, US. *Environ Res Lett* 14:054011. <https://doi.org/10.1088/1748-9326/ab148e>
- Yilmaz M, Tosunoglu F (2019) Trend assessment of annual instantaneous maximum flows in Turkey. *Hydrol Sci J J Sci Hydrol* 64:820–834. <https://doi.org/10.1080/02626667.2019.1608996>
- Yin Y, Xu Y, Ying C (2009) Relationship between flood/drought disasters and ENSO from 1857 to 2003 in the Taihu Lake Basin, China. *Quat Int* 208:93–101
- Yu Y, Shen Y, Wang J, Wei Y, Deng H (2021) Assessing the response of vegetation change to drought during 2009–2018 in Yunnan Province, China. *Environ Sci Pollut Res* 28:47083–47085. <https://doi.org/10.1007/s11356-021-14804-7>

- Zhao H, Pan X, Wang Z, Jiang S, Liang L, Wang X, Wang X (2019) What were the changing trends of the seasonal and annual aridity indexes in northwestern China during 1961–2015? *Atmos Res* 222:154–162. <https://doi.org/10.1016/j.atmosres.2019.02.012>
- Zhou Q, Jiang H, Wang J, Zhou J (2014) A hybrid model for PM_{2.5} forecasting based on ensemble empirical mode decomposition and a general regression neural network. *Sci Total Environ* 496:264–274. <https://doi.org/10.1016/j.scitotenv.2014.07.051>
- Zveryaev II (2006) Seasonally varying modes in long-term variability of European precipitation during the 20th century. *J Geophys Res-Atmos* 111:D21. <https://doi.org/10.1029/2005JD006821>

Publisher's note Springer Nature remains neutral with regard to jurisdictional claims in published maps and institutional affiliations.